Supplementary information for "Tunable symmetry breaking in a hexagonal-stacked moiré magnet"

Zeliang Sun*,[1], Gaihua Ye*,[2], Xiaohan Wan[1], Ning Mao[3], Cynthia Nnokwe[2], Senlei Li[4], Nishkarsh Agarwal[5], Siddhartha Sarkar[6], Zixin Zhai[7], Bing Lv[7], Robert Hovden[5], Chunhui Rita Du[4], Yang Zhang[8,9], Kai Sun[1], Rui He[+,2], Liuyan Zhao[+,1]

[1] Department of Physics, University of Michigan, Ann Arbor, MI, 48109, USA

[2] Department of Electrical and Computer Engineering, Texas Tech University, Lubbock, TX, 79409, USA

[3] Max Planck Institute for Chemical Physics of Solids, Nöthnitzer Straße 40, 01187 Dresden, Germany

[4] School of Physics, Georgia Institute of Technology, Atlanta, GA, 30332, USA

[5] Department of Materials Science and Engineering, University of Michigan, Ann Arbor, MI, 48109, USA

[6] Max Planck Institute for the Physics of Complex Systems, Nöthnitzer Straße 38, 01187 Dresden, Germany

[7] Department of Physics, the University of Texas at Dallas, Richardson, TX, 75089, USA

[8] Department of Physics and Astronomy, University of Tennessee, Knoxville, TN, 37996, USA

[9] Min H. Kao Department of Electrical Engineering and Computer Science, University of Tennessee, Knoxville, Tennessee 37996, USA

* The authors contribute equally

+ corresponding authors: Liuyan Zhao (lyzhao@umich.edu); Rui He (rui.he@ttu.edu)

Supplementary Information Note 1. Stacking configuration of rhombohedral-staked (R-stacked) and hexagonal-stacked (H-stacked) CrI_3.

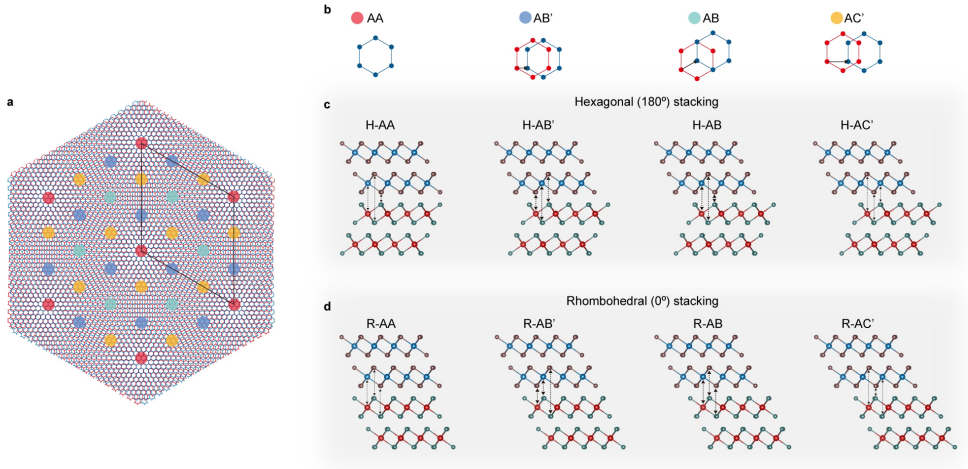

Fig. S1| Stacking configuration of R-staked and H-stacked CrI_3. a, The moiré superlattice of twisted double bilayer CrI_3 at the interface between two 2L CrI_3. Four representative stacking geometries are shown: AA (red dot), AB' (blue dot) AB (green dot) and AC' (yellow dot). **b**, Schematic structure of different stacking geometries shown in **a**. Here, only Cr atoms are shown, and the arrows indicate the shift vector between two CrI_3 layers. **c,** The side views of different stacking geometries of H-stacked double bilayer CrI_3. **d,** The side views of different stacking geometries of R-stacked double bilayer CrI_3.

Supplementary Information Note 2. Calculated interlayer exchange coupling energy for H-stacked double bilayer CrI_3.

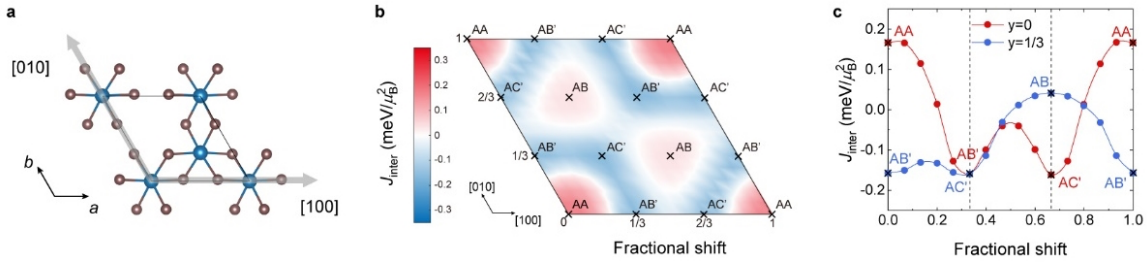

Fig. S2|Interlayer exchange energy of H-stacked double bilayer CrI_3. a, The crystal structure of monolayer CrI_3 in the *ab* plane. The shift vector [*x y*] defines the fractional coordinates of relative shift of the unit cell of one CrI_3 layer with respect to the unit cell in the neighboring layer of the interface, in which *x* is the fractional shift along [100] direction and *y* the fractional shift along [010] direction. For example, [0 0] is AA site, [1/3 0] is AB' site, [2/3 0] is AC' site, and [2/3 1/3] is AB site. **b,** Interlayer exchange energy of H-stacked double bilayer CrI_3 at different shift vectors. Four represent stacking sites AA, AB', AC' and AB are marked in the 2D map. **c,** The interlayer exchange energy along two high-symmetry line-cut [*x* 0] (red line) and [*x* 1/3] (blue line) of **b**.

J_{inter} (meV/μ_B^2)	AA	AB	AB'	AC'
R-stacking	-0.102	-0.314	0.039	0.063
H-stacking	0.166	0.040	-0.158	-0.162

Table S1|Calculated interlayer exchange energy at four sites: AA, AB, AB' and AC' in R-stacked and H-stacked double bilayer CrI_3, respectively.

Supplementary Information Note 3. Calculated stacking energy for H-stacked double bilayer CrI_3.

In this section, we discuss the formation of highly uniform moiré superlattice from the stacking energy in H-tDB CrI_3. Figure S3 shows the calculated stacking energy for H-stacked double bilayer CrI_3 at different stacking sites. It shows that the AA site has the largest stacking energy, then AB site, and the stacking energy of AB' and AC' are degenerate and lowest. In the moiré superlattice, the AA site is surrounded by the alternating degenerate AB' and AC' site (Fig. S1a), forming six-fold degenerate stacking energy distribution. Due to the more uniform distribution of stacking energy in the moiré superlattice, the H-tDB CrI_3 is expected to form higher-quality moiré superlattice.

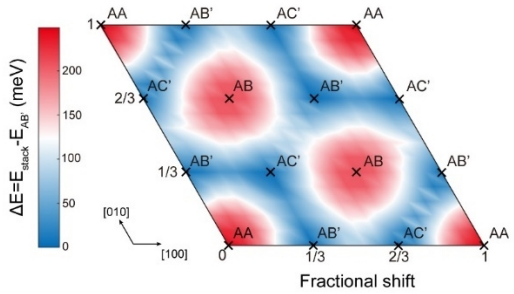

Fig. S3|Calculated stacking energy for H-stacked double bilayer CrI_3 at different shift vectors.

Supplementary Information Note 4. Derivation of Raman tensor.

This section shows our calculation of the Raman tensors of H-tDB CrI_3. As we used backscattering geometry with incident light perpendicular to the *ab* plane in the experiment, the Raman tensor *R* is a 2×2

matrix. The measured Raman intensities (I) can be expressed as: $I \propto \left|\langle \hat{e}_f | R | \hat{e}_i \rangle\right|^2$, where $\hat{e}_i$ and $\hat{e}_f$ are the unit polarization vectors of the incident and scattered light, respectively. In the parallel channel, in which $|\hat{e}_i\rangle$ is parallel to $|\hat{e}_f\rangle$, the incident and scattered light can be written as $|\hat{e}_i\rangle = \binom{cos\theta}{sin\theta}$, and $|\hat{e}_f\rangle = \binom{cos\theta}{sin\theta}$. In the crossed channel, in which $|\hat{e}_i\rangle$ is perpendicular to $|\hat{e}_f\rangle$, the incident and scattered light can be written as $|\hat{e}_i\rangle = \binom{cos\theta}{sin\theta}$, and $|\hat{e}_f\rangle = \binom{-sin\theta}{cos\theta}$. Here, we only show the derivation of Raman tensor and fitted intensity for U_1 mode, the fitted intensity of U_2-U_4 modes can be derived with the same Raman tensor.

First, in the AFM state of 2L CrI_3, only one peak U_1 shows in parallel channel with same intensity at different incident light angles (Table S2), consequently the Raman tensor in 2L CrI_3 for U_1 is $\begin{pmatrix} a & 0 \\ 0 & a \end{pmatrix}$. The intensity $I_{U_1,2L}^{parallel} \propto |(cos\theta, sin\theta)\begin{pmatrix} a & 0 \\ 0 & a \end{pmatrix}\binom{cos\theta}{sin\theta}|^2 = a^2$, and $I_{U_1,2L}^{crossed} \propto |(-sin\theta, cos\theta)\begin{pmatrix} a & 0 \\ 0 & a \end{pmatrix}\binom{cos\theta}{sin\theta}|^2 = 0$. We note that although the point group of 2L CrI_3 is C_{2h}, the Raman tensor of U_1 shows the A_g symmetry of the D_{3d} point group of monolayer CrI_3, which is attributed to the weak interlayer coupling. In 180°-tDB CrI_3, the pattern for U_1 in crossed channel shows four lobs with same intensity (fig. 4m in the main text), which breaks the rotational symmetry, and the Raman tensor is $\begin{pmatrix} a & 0 \\ 0 & b \end{pmatrix}$. Thus, the intensity $I_{U_1,180}^{parallel} \propto |(cos\theta, sin\theta)\begin{pmatrix} a & 0 \\ 0 & b \end{pmatrix}\binom{cos\theta}{sin\theta}|^2 = |\frac{a+b}{2} + \frac{a-b}{2}cos2\theta|^2 = \frac{1}{8}(a-b)^2 cos4\theta + \frac{1}{2}(a^2-b^2)cos2\theta + \frac{1}{8}(3a^2+2ab+3b^2)$, and $I_{U_1,180}^{crossed} \propto |(-sin\theta, cos\theta)\begin{pmatrix} a & 0 \\ 0 & b \end{pmatrix}\binom{cos\theta}{-sin\theta}|^2 = |\frac{a-b}{2}sin2\theta|^2 = -\frac{1}{8}(a-b)^2 cos4\theta + \frac{1}{8}(a-b)^2$. For the twist angle of 181.1, 183 and 185, the patterns of U_1 in the crossed channel show four lobes with unequal intensity. Thus, the Raman tensor contains antisymmetric real off-diagonal Ramman tensor. Due to the nonzero Raman circular dichroism $I_{LL} \neq I_{RR}$, an antisymmetric complex off-diagonal Ramman tensor also appears in the Raman tensor. Consequently, the Raman tensor for U_1 is $\begin{pmatrix} a & c+di \\ -c-di & b \end{pmatrix}$. Here, we show the fitting process of 183° H-tDB CrI_3. The intensity $I_{U_1,183}^{parallel} \propto |(cos\theta, sin\theta)\begin{pmatrix} a & c+di \\ -c-di & b \end{pmatrix}\binom{cos\theta}{sin\theta}|^2 = |\frac{a+b}{2} + \frac{a-b}{2}cos2\theta|^2 = \frac{1}{8}(a-b)^2 cos4\theta + \frac{1}{2}(a^2-b^2)cos2\theta + \frac{1}{8}(3a^2+2ab+3b^2)$, and $I_{U_1,183}^{crossed} \propto |(-sin\theta, cos\theta)\begin{pmatrix} a & c+di \\ -c-di & b \end{pmatrix}\binom{cos\theta}{sin\theta}|^2 = |c+id+\frac{a-b}{2}sin2\theta|^2 = -\frac{1}{8}(a-b)^2 cos4\theta + (a-b)csin2\theta + \frac{1}{8}(a-b)^2 + c^2 + d^2$. In the circular basis, for 183°-tDB CrI_3, $I_{U_1,183}^{LL} \propto |(1,-i)\begin{pmatrix} a & c+di \\ -c-di & b \end{pmatrix}\binom{1}{i}|^2 = (a+b-2d)^2 + 4c^2$ and $I_{U_1,183}^{RR} \propto |(1,i)\begin{pmatrix} a & c+di \\ -c-di & b \end{pmatrix}\binom{1}{-i}|^2 = (a+b+2d)^2 + 4c^2$. Because $I_{U_1,183}^{LL} \neq I_{U_1,183}^{RR}$, Raman circular

dichroism is shown. The same fitting analysis also applies to the 181.1° and 185°-tDB CrI_3 samples. We summarize the Raman tensors and polarization-dependent intensity pattern in Table S2.

	Raman tensor	parallel channel	crossed channel	Raman circular dichroism
2L	$\begin{pmatrix} a & 0 \\ 0 & a \end{pmatrix}$	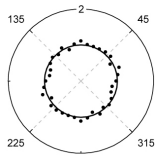		$I_{LL}=I_{RR}=4\|a\|^2$
180°	$\begin{pmatrix} a & 0 \\ 0 & b \end{pmatrix}$	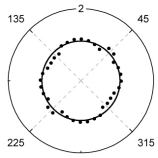	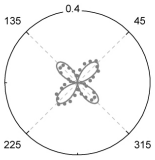	$I_{LL}=I_{RR}=\|a+b\|^2$
183°	$\begin{pmatrix} a & c+id \\ -c-id & b \end{pmatrix}$	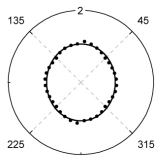	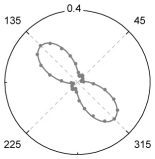	$I_{LL}=(a+b-2d)^2+4c^2$ $I_{RR}=(a+b+2d)^2+4c^2$ $I_{LL}\neq I_{RR}$

Table S2|Raman tensor of 180°, 183° H-tDB and 2L CrI_3.

Supplementary Information Note 5. Calculations of magnetic ground state of H-tDB CrI_3.

In this section, we discuss the ground spin state of H-tDB CrI_3 at different twist angles. Using numerical minimization, we identified the ground spin state by finding the spin structure with the lowest total energy of the Hamiltonian given in the method section of the main text. To account for the effect of possible structural distortion of iodine octahedral cages caused by the moiré superlattice in tDB CrI_3, we varied the magnetic anisotropy $\gamma_{\text{moiré}}$ for the middle two layers, as well as for all the four layers, in the calculations.

In Figure S4a, we plot the $J_{\text{moiré}}$ function, fitted from the shift vector-dependent J_{inter} as shown Fig. S2b. By minimizing the energy, we obtain the ground state spin configuration at different twist angles and $\gamma_{\text{moiré}}$ with a triangular grid of $L \times L \times 4 = 100 \times 100 \times 4$. The phase diagram of H-tDB CrI_3 with varied twist angle and magnetic anisotropy $\gamma_{\text{moiré}}$ is shown in Fig. S4c and S4d, where the horizontal axis is $\gamma_{\text{moiré}} - 1$ and vertical axis is the twist angle. The phase diagrams in Figs. S4c (varying $\gamma_{\text{moiré}}$ for the middle two layers at the interface) and S4d (varying $\gamma_{\text{moiré}}$ throughout all four layers) are qualitatively similar, featuring three prominent distinct phases (see schematic spin configurations of different phases in Fig. S4b), which we label as the twisted phase with one out-of-plane domain wall (O-1DW), the twisted phase with

two in-plane domain walls (I-2DW), and the collinear phase (CL, no domain walls). At large twist angles, the middle two layers favor FM ground states, showing CL phase. The middle two layers favor FM ground states at large twist angles because the large area of AB' region with FM interlayer exchange coupling dominates.

Notably, for $1.00445 < \gamma_{\text{moiré}} < 1.00846$, the I-2DW phase appears over a broad range of twist angles. I-2DW phase features in-plane domains (major component of spins within the domain are in-plane) at H-AA. As shown in Fig. S4e, in the I-2DW phase ($1.00445 < \gamma_{\text{moiré}} < 1.00846$), the net magnetization $\langle m_z \rangle$ is always of order 0.01, with 1 representing the magnetic moment of Cr^{3+}. As a reference, the computed net $\langle m_z \rangle$ in 1.1° R-tDB CrI_3 is of order 0.1 (ref. [1]). When $\gamma_{\text{moiré}}$ further increases, the favored ground state is O-1DW phase, which is similar to the ground state of R-tDB CrI_3 with twist angle around 1.1° (ref. [1]). The net magnetization $\langle m_z \rangle$ in O-1DW phase also shows larger values compared to I-2DW phase. From the calculation results, the experimentally observed moiré spin textures in H-tDB CrI_3 with twist angle 181.1°~185° likely corresponds to the magnetic ground state of I-2DW phase, with in-plane domains and near zero net magnetization. The in-plane domains break C_3 rotational symmetry and mirror symmetry, and the allowed but very small net magnetization breaks the time-reversal symmetry but does not cause a large MCD signal. The combination of them is consistent with the form of Raman tensor obtained from experiment.

To compare, we also calculated the phase diagram considering all 4 layers with $\gamma_{\text{moiré}}$. We found that it is similar to the phase diagram considering only middle two layers with $\gamma_{\text{moiré}}$, except the ground states feature a 4-layer in-plane domain walls (I-4DW) between 181° ~181.5° at small $\gamma_{\text{moiré}}$ and the ground state becomes twisted phase with 2 out-of-plane domain walls (O-2DW) around 180.8° (Fig. S4d). The calculated $< m_z >$ with $\gamma_{\text{moiré}}$ of all 4 layers are shown in Fig. s4f.

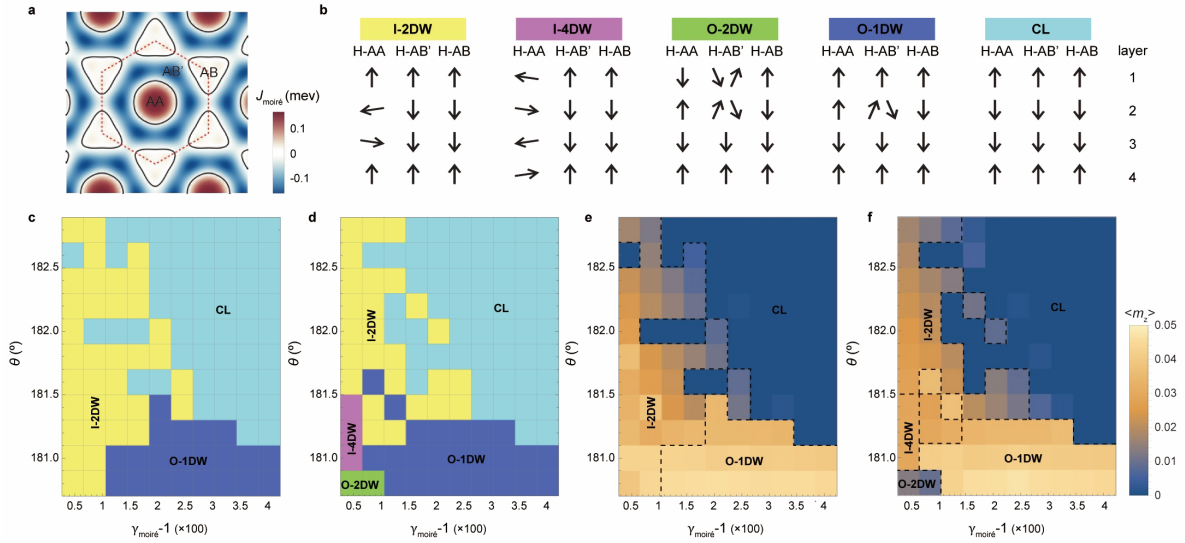

Fig. S4|Calculation results of magnetic ground state of H-tDB CrI_3. a, Fitted moiré interlayer coupling energy $J_{moiré}$. H-AA and H-AB have AFM coupling while H-AB' has FM coupling. The black lines label the place where $J_{moiré}$=0. **b,** Schematic spin configurations of different phases in **c** and **d**. **c,** Phase diagram of H-tDB CrI_3 with varied twist angles and magnetic anisotropy $\gamma_{moiré}$ of middle two layers. **d,** Phase diagram of H-tDB CrI_3 with varied twist angles and magnetic anisotropy $\gamma_{moiré}$ of all four layers. **e**, Net magnetization $<m_z>$ of H-tDB CrI_3 with varied twist angles and magnetic anisotropy $\gamma_{moiré}$ of middle two layers. **f**, Net magnetization $<m_z>$ of H-tDB CrI_3 with varied twist angles and magnetic anisotropy $\gamma_{moiré}$ of all four layers.

Having clarified the magnetic ground states at zero magnetic field, we further calculated the energy of different spin configurations and their out-of-plane magnetization (m_z) under magnetic field. First, we found that under magnetic field, the ground state I-2DW phase at zero field first transits to an intermediate phase with one out-of-plane domain walls with large m_z~0.43 (O-1DW-II, spin alignment is shown in Fig. S5). With further increasing field above 0.7 T, the ground state evolves to FM phase. Second, although the ground state at zero field is I-2DW phase, the ground state becomes O-1DW phase and the first excited phase becomes I-2DW phase when the field increases to 0.08 T. The energy difference between I-2DW and O-1DW are smaller than 0.1% between ±0.36 T. And m_z of O-1DW phase under magnetic field is smaller than O-1DW-II phase. Based on the above calculation results, we can get the evolution of m_z of H-tDB CrI_3 under magnetic field (Fig. S5). The initial ground state at zero magnetic field is I-2DW phase (yellow dot in Fig. S5) with near zero m_z. With increasing magnetic field (below 0.7 T), I-2DW phase first transits to O-1DW-II phase (red dot in Fig. S5) with a larger m_z at B_m~0.1 T, which shows an abrupt upturn of m_z curve above B_m. When the magnetic field is larger than 0.7, the spin state enters FM phase (cyan dot in Fig. S5). When decreasing the magnetic field below 0.7 T, the spin state first enters O-1DW phase (blue dot in Fig. S5) with smaller m_z than O-1DW-II phase, thus forming a magnetization hysteresis loop as observed in the experimental data. As field further decreases below 0.1 T (B_m), the spin state re-enters the ground state (I-2DW).

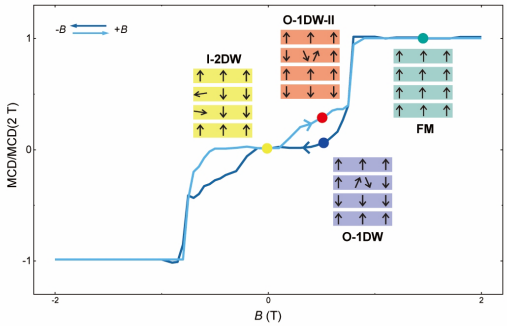

Fig. S5|Evolustion of spin state of H-tDB CrI_3 under magnetic field.

Reference

1. Xie, H. *et al.* Evidence of non-collinear spin texture in magnetic moiré superlattices. *Nat. Phys.* **19**, 1150-1155 (2023).